MathematicS

MathS In A.

In Action

Simon Garnotel, Stéphanie Salmon & Olivier Balédent

Numerical Modeling of the Intracranial Pressure using Windkessel Models

Volume 8 (2017), p. 9-25.

<http://msia.cedram.org/item?id=MSIA_2017__8_1_9_0>

MathematicS In Action
Vol. 8, 9-25 (2017)

Numerical Modeling of the Intracranial Pressure using Windkessel Models

Simon Garnotel
Stéphanie Salmon
Olivier Balédent

* Laboratoire BioFlowImage, Université de Picardie Jules Verne, France
E-mail address: simon.garnotel@u-picardie.fr
** Laboratoire de Mathématiques de Reims, Université de Reims Champagne-Ardenne, France
E-mail address: stephanie.salmon@univ-reims.fr
*** Unité de Traitement de l'Image, CHU Amiens-Picardie, France
E-mail address: olivier.baledent@chu-amiens.fr.

Abstract

The intracranial pressure (ICP) is an important factor in the proper functioning of the brain. This pressure is needed to be constantly regulated, since an abnormal elevation can be quite dangerous. In this article, we develop some numerical tools to better understand the regulation of this pressure. In particular, as it is impossible to measure the ICP in a non-invasive way, these numerical tools can allow to estimate values of the ICP. In addition, we propose to compute the dynamics of the cerebrospinal fluid (CSF), taking into account the connected environment of the skull and the arterio-venous flows. A computational fluid dynamics model in two dimensions is developed for the cerebrospinal fluid system, with Windkessel type boundary conditions. This model shows that the dynamics can impact the distribution of the CSF in the different compartments of the cerebrospinal system.

1. Introduction

The intracranial pressure (ICP) is an important clinical parameter for the proper functioning of the brain. The ICP is the pressure in the water-like fluid, mainly composed of water (99% of water and 1% of proteins, glucose, minerals), that is in and around the brain, namely the cerebrospinal fluid (CSF). This pressure results from the interaction between the brain parenchyma, the venous, the arterial and the CSF volumes inside the skull, assumed incompressible.

The cerebrospinal system is composed of the cerebral ventricles, the cerebral subarachnoid spaces (SAS) and the spinal SAS: all of these compartments contain CSF and are connected, see Fig. 1.1. Cerebral ventricles and SAS are connected by a tiny tube, called the aqueduct of Sylvius. All of these compartments have their own elasticity, called compliance. The CSF oscillates in the system, between the cerebral and the spinal compartments, at a frequency related to the cardiac pulse and thus to the blood flow entering and exiting the brain [4, 3].

The volume and distribution of CSF in the central nervous system is involved in many pathologies inducing ICP alterations. Non-communicating hydrocephalus is the most viewable by imaging techniques and well known of these pathologies: it is characterized by a large increase of the cerebral ventricles [15] and can also induce significant redistribution of CSF pulsations within the SAS to the ventricular system [3, 24]. First studies on the global cerebrospinal system were carried out mainly to understand the behavior of these obstructive pathologies. CSF alterations as hydrocephalus are directly related to unbalance between CSF production and resorption in

Keywords: Intracranial pressure, Stokes equations, Finite element method, Windkessel models.
2010 *Mathematics Subject Classification:* 76Z05.

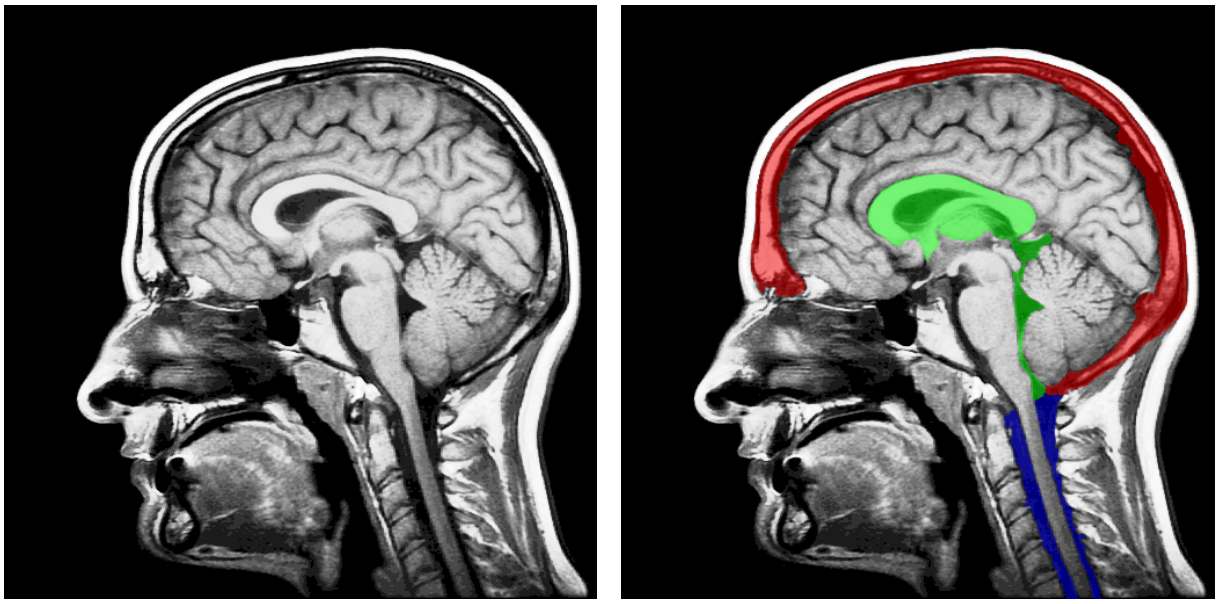

(a) Morphological MRI (b) Colored MRI

Figure 1.1. (a). Morphological MRI of the cerebrospinal system. (b). Schematic representation of cerebral ventricles (green), cerebral SAS (red) and spinal SAS (blue).

a global static approach of the cerebrospinal system. Part of hydrocephalus origin is well identified as complete obstruction of the aqueduct of Sylvius or partial obstruction of the SAS, due to subarachnoid hemorrhage or meningitis. However, part of physiopathology of hydrocephalus patients is still not understood [15]: indeed some idiopathic hydrocephalus cases are reported where no obstruction is seen.

As the intracranial pressure is difficult to measure in a non-invasive way and as its regulation is quite hard to understand, we first build a simplified numerical model in order to understand the dynamics of the CSF, its impact on the ICP and on the cerebral blood flow. We also aim to identify the parameters that govern the dynamic: frequency or amplitude of the blood flow entering the brain, for instance.

1.1. State of the art

Electrical modeling. Historically, electrical modeling of the ICP has been proposed that uses an electrical/mechanical analogy in a static approach (or at equilibrium) of the global cerebrospinal system. The first and most popular studies on the ICP have been proposed by Marmarou *et al.* [16, 17]. These studies considered a global static approach of the cerebrospinal system and used an electrical modeling to describe the secretion/absorption process of the CSF, see Fig. 1.2. The formation site corresponds to the choroid plexus in the ventricles, the absorption site corresponds to the arachnoid granulations and the storage site to the global elasticity of the system, which represents its capacity to increase (respectively decrease) its volume with an increase (respectively decrease) of the pressure. This process controls the ICP in a long-term. Some relations between ICP and CSF volume have been established:

$$ICP(t) = P_0.e^{E.V(t)} \tag{1.1}$$

where P_0, E and V are respectively the initial pressure, the cerebrospinal system elastance and the difference between the initial CSF volume and the overage CSF volume, during an injection test, for example.

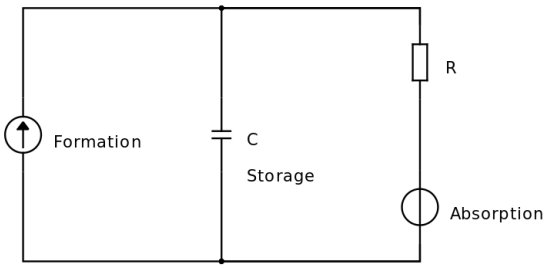

Figure 1.2. Representation of the electrical model of Marmarou's studies. C is the intracranial compliance, R the absorption resistance.

Others studies using electrical modeling have been carried out, as the study proposed by Ursino *et al.* [25], where a global representation of the cerebrospinal system including the surrounding arterial and venous network was developed, to understand the auto-regulation of the intracranial pressure. Inter alia, simulation of injection test were made for different parameters, in order to validate the model and study ICP response.

Electrical models have the benefits to be fast; however accuracy is poor and they involve many parameters that are difficult to measure or estimate.

Mechanical modeling. A physiological phantom has been realized [5], to reproduce interactions between arterio-venous pulse and CSF pulse, using mechanical devices as pumps, see a scheme in Fig. 1.3. This phantom has shown that CSF is driven by arterio-venous pulses and that ICP depends on the system parameters. The difficulty to modify the parameters in this phantom, other than the pump frequency, is a limit to this study. Numerical simulations can allow to obtain some complementary information.

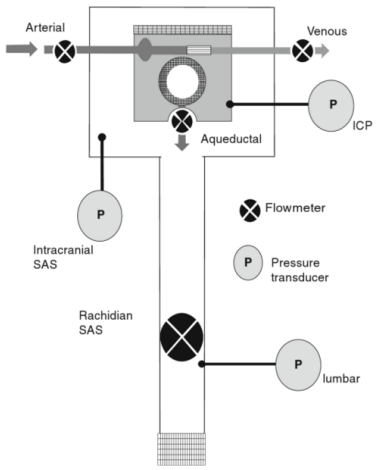

Figure 1.3. Representation of the Bouzerar's phantom [5].

Numerical modeling. Numerical modeling came with the improvement of computer resources. It uses physics-based equations, time-dependent or not, and simplified or realistic geometries.

Only few approaches devoted to the cerebrospinal system have studied the influence of CSF dynamics in the repartition of the CSF between the two main intracranial compartments: the

Table 1.1. CSF parameters.

Parameter		Value	Unity
Density	ρ	10^{-3}	$g.mm^{-3}$
Viscosity	μ	10^{-3}	Pa.s

cerebral ventricular compartment at the center of the brain and the cerebral SAS surrounding the parenchyma. These two compartments are directly connected to the third CSF compartment: the spinal canal, outside the brain, which gives compliance to the cranium during the systolic vascular cerebral expansion at each cardiac cycle [12].

Recent studies have been proposed with 2D or 3D models using the finite element method, for instance the one developed by Alperin *et al.* [2]. It used a schematic representation of the spinal cord to model the CSF flow in the spinal SAS. This study used a physics-based fluid equation, namely the time-dependent Stokes equation and the output of the spinal SAS was considered as a free output.

Other studies used porous media to model the entire cerebral compartments: cerebral ventricles, cerebral SAS and the brain, like in Linninger *et al.* study [14] where numerical velocity, obtained using the time-dependent Navier-Stokes equations and a Darcy's law, was compared to MRI measurements to look for a clinical indication.

1.2. Our numerical model

Numerical simulations allow better accuracy, by taking advantage of the use of physics-based equations; however they require high computer resources and the simulation time is often long, especially for fluid-structure interaction computation. In this study, we use a simulation containing 2D models with physics-based equations, namely the time-dependent Stokes equations, and some electrical models for the boundary conditions: the Windkessel models. This technique allows us to have simulation results in a reasonable time.

In the sequel, the CSF is modeled as an incompressible fluid following the time-dependent Stokes equations Eq. (2.1). Indeed, fluid parameters of the CSF (at 37°C) are used, see Tab. 1.1, and the system is in coated position, so we neglect gravity in a first approach.

As the real geometry is quite complex, and in order to understand the dynamics between the different compartments, we first model the cerebrospinal system by a 2D bifurcation that takes into account the three main compartments of the cerebrospinal system: cerebral ventricles, cerebral SAS and spinal SAS in the confined environment of the skull, see Fig. 1.4. Arterial pulse, that brings blood to the brain at each cardiac cycles, increases the total volume contained in the rigid skull. It then forces CSF to exit the brain and though the pressure increases. Thanks to this first simplified model, we aim to better understand the CSF distribution in the different compartments and its impact on the ICP.

In blood flow simulations, as only a part of the network is considered, it is necessary to impose artificial boundary conditions to model the remaining network. These artificial boundary conditions are classically defined by considering an analogy with an electrical model [26], which is called the Windkessel model [23], see Tab. 1.2. In this article, we will consider such a Windkessel model to take into account interactions between cerebral ventricles and cerebral SAS in the confined environment of the skull and the impact of blood flow entering the brain.

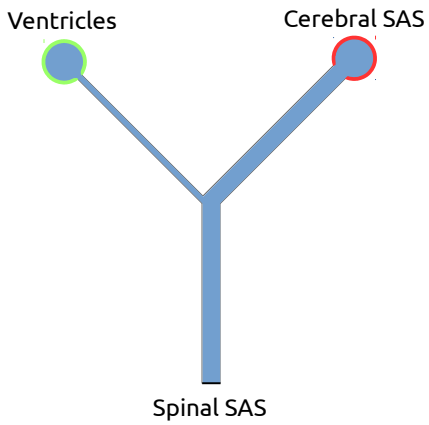

Figure 1.4. Modeling of the cerebrospinal system.

Table 1.2. Electrical/mechanical analogy.

Electrical		Mechanical	
Current	i	Flow rate	Q
Voltage	U	Pressure	p
Resistance	R	Resistance	R
Capacity	C	Compliance	C

2. The Stokes equations and boundary conditions

2.1. The Stokes equations

The fluid simulation is performed by solving the time-dependent incompressible Stokes equations Eq. (2.1) using the finite element method.

$$\rho\frac{\partial \mathbf{u}}{\partial t} + \quad p - \mu\Delta\mathbf{u} = \mathbf{f} \qquad \text{in } [0,T]\times\Omega \tag{2.1a}$$

$$\operatorname{div}(\mathbf{u}) = 0 \qquad \text{in } [0,T]\times\Omega \tag{2.1b}$$

$$\mathbf{u} = \mathbf{u}_D \qquad \text{on } [0,T]\times\Gamma_D \tag{2.1c}$$

$$\mu\frac{\partial \mathbf{u}}{\partial \mathbf{n}} - p\mathbf{n} = \mathbf{g}_N \qquad \text{on } [0,T]\times\Gamma_N \tag{2.1d}$$

$$\mathbf{u}_{|t=0} = \mathbf{u}^0 \qquad \text{in } \{0\}\times\Omega \tag{2.1e}$$

Variable $\mathbf{u}$ is the velocity vector and p the pressure, ρ is the density, μ the dynamic viscosity of the fluid and $\mathbf{f}$ an external force taken here equal to zero (gravity is neglected in a first approach). The two-dimensional domain Ω, modeling the geometry of the bifurcation, has a boundary $\partial\Omega$ split in Γ_D and Γ_N, where we impose respectively $\mathbf{u}_D$ (Dirichlet boundary condition) and $\mathbf{g}_N$ (Neumann boundary condition) and T the final time of the study. The initial condition on the velocity is called $\mathbf{u}^0$. Dirichlet conditions are imposed on the inlet (spinal SAS) and on the wall, Neumann conditions are imposed on the outlets (cerebral ventricles and cerebral SAS).

We solve the Stokes equations using the finite element method with the open-source software FreeFem++ [13]. The difficulty for solving the Stokes equations is the zero divergence condition Eq. (2.1b). We consider here a classical algorithm [20]: the zero divergence condition involves a

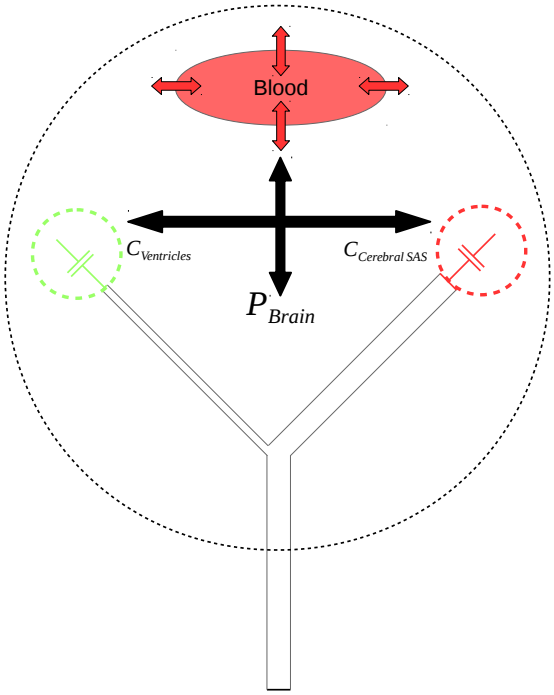

Figure 2.1. **CSF Windkessel Model.** The cerebrospinal system is modeled by a bifurcation with two deformable compartments: cerebral ventricles and cerebral SAS. These compartments interact each other and equally with the cerebral blood.

mixed weak form that can be managed by choosing compatible spaces for the velocity and the pressure, respecting the so-called inf-sup condition. To speed-up the resolution, this method is coupled with an iterative Uzawa Conjugate Gradient algorithm [22] with a Cahouet-Chabart preconditionner [6].

2.2. Boundary conditions

The different interactions considered in the cerebrospinal system are shown on Fig. 2.1.

In our model, spinal SAS is considered as an input, cerebral SAS and cerebral ventricles are considered as outputs, walls are considered as a non-slip boundary.

Spinal SAS and wall conditions are imposed using a Dirichlet boundary condition, so the boundary Γ_D is split into Γ_{in} and Γ_{wall}. On Γ_{in}, we impose the velocity profile $\mathbf{u}_{in}$ computed from phase contrast MRI (PC-MRI) data obtained in the BioFlowImage laboratory [19]. On Γ_{wall} a null velocity is imposed.

Cerebral SAS and cerebral ventricles conditions are imposed using a Neumann boundary condition: so the boundary Γ_N is split into Γ_{SAS} and Γ_{Vent}. On each of these boundaries, a Windkessel model is imposed, *i.e.* a tensor containing the pressure (P_{SAS} and P_{Vent}). As cerebral SAS and cerebral ventricles are deformable compartments, they are modeled by capacities (or compliances). Considering the electrical/mechanical analogy in Tab. 1.2, the Windkessel's pressure is a function of capacity and flow during time in the following way:

$$P_{SAS}(t) = \frac{1}{C_{SAS}(t)} \int_0^t Q_{SAS}(s)ds, \tag{2.2}$$

$$P_{Vent}(t) = \frac{1}{C_{Vent}(t)} \int_0^t Q_{Vent}(s)ds, \tag{2.3}$$

where $Q_{SAS}(t)$ and $Q_{Vent}(t)$ are respectively cerebral SAS and cerebral ventricles flows.

To take into account the confined environment and the arterio-venous volume, we consider the brain pressure $P_{Brain}(t)$ as a function of the volumes in the expression of compliances:

$$C_{Vent}(t) = \frac{C^0_{Vent}}{P_{Brain}(t)} \text{ with } C^0_{Vent} \quad \mathbb{R}, \tag{2.4}$$

$$C_{SAS}(t) = \frac{C^0_{SAS}}{P_{Brain}(t)} \text{ with } C^0_{SAS} \quad \mathbb{R}. \tag{2.5}$$

In a first approach, we consider the brain pressure $P_{Brain}(t) = P_0 e^{kV(t)}$, with $P_0,\ k \quad \mathbb{R}$ and $V(t) = V_{Vent}(t) + V_{SAS}(t) + V_{Blood}(t)$, as in Marmarou's static study of the cerebrospinal system [17]. The volumes V_{Vent} and V_{SAS} are cerebral ventricles and cerebral SAS volumes respectively, and V_{Blood} is the arterio-venous volume computed from PC-MRI data that were obtained in the BioFlowImage laboratory.

2.3. Weak form and discretization

In order to present the computational approach, we introduce the functional spaces for the velocity and the pressure:

$$\begin{aligned}
&V^0 = \{\mathbf{v} \quad H^1(\Omega)^2, \mathbf{v}_{|\Gamma_D} = 0\} && V^D = \{\mathbf{v} \quad H^1(\Omega)^2, \mathbf{v}_{|\Gamma_D} = \mathbf{u}_D\}\\
&V^0_t = L^2([0,T]; V^0) && V^D_t = L^2([0,T]; V^D)\\
&Q = L^2(\Omega)\\
&Q_t = L^2([0,T]; Q)
\end{aligned} \tag{2.6a}$$

The semi-discrete variational formulation needed for the finite element method is the following: find $(\mathbf{u}, p) \quad V^D_t \times Q_t$ such that for all $(\mathbf{v}, q) \quad V^0_t \times Q_t$:

$$\rho \int_\Omega \frac{\partial \mathbf{u}}{\partial t}.\mathbf{v} + \int_\Omega p.\mathbf{v} - \mu \int_\Omega \Delta\mathbf{u}.\mathbf{v} = \int_\Omega \mathbf{f}.\mathbf{v} + \int_{\Gamma_N} \mathbf{g}_N.\mathbf{v} \tag{2.7a}$$

$$\int_\Omega \mathrm{div}(\mathbf{u})q = 0 \tag{2.7b}$$

with:

$$\mathbf{g}_N = \begin{cases} \left(\frac{1}{C_{Vent}(t)} \int_0^t \mathbf{u}.\mathbf{n}ds\right)\mathbf{n} & \text{on } \Gamma_{\text{Vent}} \\ \left(\frac{1}{C_{SAS}(t)} \int_0^t \mathbf{u}.\mathbf{n}ds\right)\mathbf{n} & \text{on } \Gamma_{\text{SAS}} \end{cases} \tag{2.8}$$

Let $\mathcal{T}$ be a triangulation of the domain Ω, and h the maximum of the diameters of the triangles of $\mathcal{T}$. We introduce the finite-dimensional spaces $V_{t,h}^D$, $V_{t,h}^0$ and $Q_{t,h}$:

$$
\begin{aligned}
V_h^0 &= \{ \mathbf{v}_h \in [H^1(\Omega_h)]^2, \mathbf{v}_{|\Gamma_D} = 0, \ \forall K \in \mathcal{T}, \mathbf{v}_{h|K} \in [\mathbb{P}_2(K)]^2 \} \subset V^0 \\
V_{t,h}^0 &= L^2([0,T]; V_h^0) \\
V_h^D &= \{ \mathbf{v}_h \in [H^1(\Omega_h)]^2, \mathbf{v}_{|\Gamma_D} = \mathbf{u}_D, \ \forall K \in \mathcal{T}, \mathbf{v}_{h|K} \in [\mathbb{P}_2(K)]^2 \} \\
V_{t,h}^D &= L^2([0,T]; V_h^D) \\
Q_h &= \{ q \in L^2(\Omega_h), \ \forall K \in \mathcal{T}, q_{h|K} \in \mathbb{P}_1(K) \} \subset Q \\
Q_{t,h} &= L^2([0,T]; Q_h)
\end{aligned}
$$

where $\mathbb{P}_1(K)$ (resp. $\mathbb{P}_2(K)$) is the space of polynomials of degree less than or equal to 1 (resp. 2) in each triangle of $\mathcal{T}$. The discretization spaces are chosen compatible – in the sense of the so-called inf-sup condition – to cope with the divergence constraint [20, Chapter 15].

We denote by $\mathbf{u}_h^n$ and p_h^n, respectively, the velocity and pressure approximations at the time $n\Delta t$, with Δt the time step.

The fully discrete problem then reads: find $\mathbf{u}_h^{n+1} \in V_{t,h}^D$ and $p_h^{n+1} \in Q_{t,h}$ such that $\forall \mathbf{v}_h \in V_{t,h}^0$, $\forall q_h \in Q_{t,h}$:

$$
\begin{aligned}
\frac{\rho}{\Delta t} \int_\Omega \mathbf{u}_h^{n+1}.\mathbf{v}_h - \frac{\rho}{\Delta t} \int_\Omega \mathbf{u}_h^{n}.\mathbf{v}_h + \int_\Omega p_h^{n+1} \mathrm{div}(\mathbf{v}_h) - \mu \int_\Omega \Delta \mathbf{u}_h^{n+1}.\mathbf{v}_h & \\
= \int_\Omega \mathbf{f}^{n+1}.\mathbf{v}_h + \int_{\Gamma_N} \mathbf{g}_N^{n+1}.\mathbf{v}_h & \quad (2.10a) \\
\int_\Omega \mathrm{div}(\mathbf{u}_h^{n+1}) q_h = 0 & \quad (2.10b)
\end{aligned}
$$

An explicit scheme is chosen to compute the Neumann condition, $\mathbf{g}_N^{n+1}$:

$$
\mathbf{g}_N^{n+1} = \begin{cases} \frac{1}{C_{Vent}^n} \sum_{i=0}^n \Delta t \mathbf{u}^i.\mathbf{n}\, \mathbf{n} & \text{on } \Gamma_{\text{Vent}} \\ \frac{1}{C_{SAS}^n} \sum_{i=0}^n \Delta t \mathbf{u}^i.\mathbf{n}\, \mathbf{n} & \text{on } \Gamma_{\text{SAS}} \end{cases} \quad (2.11)
$$

Remark 2.1. An implicit scheme can be chosen to compute the Neumann condition, but for sake of clarity, we only detail the explicit choice.

2.4. Stability

As far as we know, we have to prove the stability of the numerical scheme, as results already proved do not take into account non-homogeneous Dirichlet condition [9]. So we need to prove that our scheme is stable (in the sense that the kinetic energy decreases) with a non-homogeneous conditions on the input and Neumann conditions using only a variable C lumped model for the outputs. The stability analysis reveals a final time dependence (inverse of $\mathcal{T}$) in the explicit coupling case that is not really representative of an optimal Courant-Friedrichs-Lewy (CFL) condition, [10]. Then, a numerical analysis of the stability reveals a non-binding CFL condition for our applications [10]. Moreover, as we use the characteristics method, no instabilities have been observed in our applications.

Remark 2.2. As mentioned above, the CFL condition is not too restrictive on the time step, so there is no need of implementing an implicit scheme for the Neumann condition.

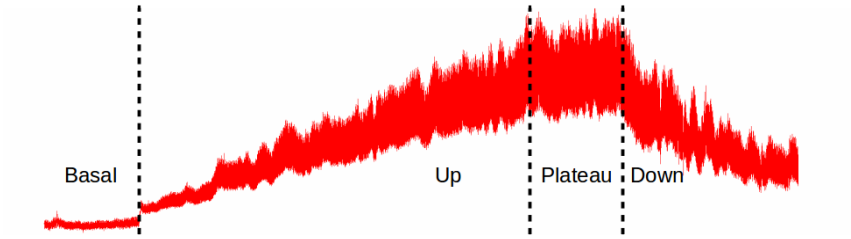

Figure 2.2. Example of pressure measurements during an injection test. Injection takes place during the Up period, when pressure rises.

Table 3.1. Simulation parameters, validation.

Parameter	Value
$Q_{SpinalSAS}$	$1 - 5.0$ mm^3.s^{-1}
ω	$0.1 - 5.0$ Hz
C^0_{SAS}	1 mm^3.Pa^{-1}
C^0_{Vent}	$0.1 - 5.0$ mm^3.Pa^{-1}
P_0	1 Pa
k	0.05

2.5. Parameters estimation

We need to fix the compliance values in the cerebral SAS and cerebral ventricles. A way to determine these compliances is to process an injection test and a flow MRI.

An injection test is a measurement of the intracranial pressure during a constant rate infusion of fluid into the SAS (cerebral or spinal) or into the cerebral ventricles. An example of pressure measurements during an injection test, with a constant rate infusion of 1 mL/min is shown in Fig. 2.2. The flow MRI (or PC-MRI) measurements allow for the calculation of the intracranial volume change (IVC), that is the sum of arterial, venous and CSF flows at the C2–C3 level (between the second and the third cervical vertebrae) integrated in time (arteries: internal carotid, vertebral; veins: internal jugular, posterior plexus, epidural; CSF: spinal SAS). The compliance value of the entire intracranial system is calculated using the following relation:

$$C = \frac{\Delta IVC}{\Delta ICP}, \tag{2.12}$$

where ΔX means $\max(X) - \min(X)$.

This global compliance has to be divided into three compliances: the cerebral ventricles, the cerebral SAS and the spinal SAS compliances.

3. Numerical results

The computed values of the Reynolds and the Strouhal numbers enforce the use of the unsteady Stokes equations, neglecting the nonlinear part. Nevertheless, all simulations have been run by solving the complete Navier-Stokes equations, but no noticeable differences were found.

3.1. Validation and impact of the input parameters

First, we want to confirm the choice of the Windkessel model. Without taking any output boundary conditions, so using free outputs, the flow distribution remains the same independently

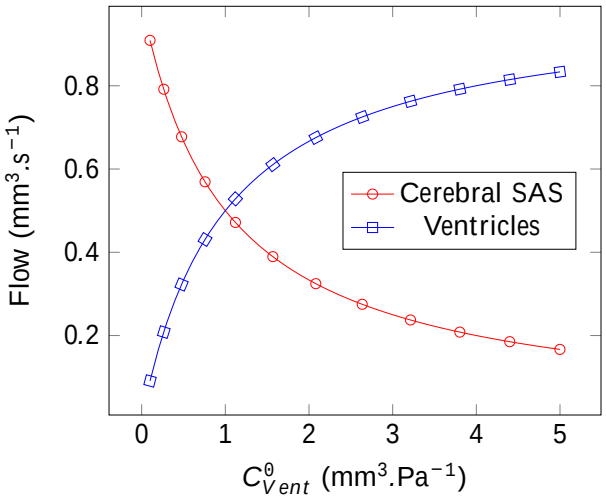

Figure 3.1. Q_{SAS} and Q_{Vent} function of C^0_{Vent}.

of the input values, with approximately 10% of the flow for the cerebral ventricles, and 90% for the cerebral SAS, as expected, see for example Fig. 3.3. This test confirms the necessity of using such Windkessel type boundary conditions to observe an impact of the input values.
Then, a constant flow is imposed at the spinal SAS with parameters taken from Tab. 3.1. The cerebral ventricles compliance value varies in $[0.1, 5.0]$, the flow frequency is taken equal to 1. The flow curves of cerebral SAS and cerebral ventricles are plotted in function of the cerebral ventricles compliance value, see Fig. 3.1. We observe that the value of the compliance has a real impact on the flow distribution: higher the cerebral ventricles compliance, higher the cerebral ventricles flow, and lower the cerebral SAS flow (according to mass conservation), which is the expected behavior.
A second experiment is carried out by imposing a pulsatile flow at the spinal SAS with parameters of Tab. 3.1 and $\omega_{Spinal\ SAS} = 1, C^0_{Vent} = 2$; the input flow amplitude varies in $[1, 50]$. The normalized maximum flow values of cerebral SAS and cerebral ventricles are plotted in function of the amplitude, see Fig. 3.2. We observe that amplitude has an impact on the CSF distribution using the variable compliances only; in the constant compliance case, no impact is seen.
A third experiment is carried out by imposing a pulsatile flow at the spinal SAS with parameters of Tab. 3.1 and $Q_{Spinal\ SAS} = 1, C^0_{Vent} = 2$; the input flow frequency varies in $[0.1, 5.0]$ and the normalized maximum flow values of cerebral SAS and cerebral ventricles are plotted in function of the heart rate, see Fig. 3.3. We observe that the heart rate has also an impact on the flow distribution: low heart rate favors cerebral ventricles while high heart rate favors cerebral SAS. Constant and variable compliances present similar results, with a small phase shift.

Based on these experiments, we have seen that both frequency and amplitude of the cardiac cycle can influence the distribution of the CSF flow in the cerebral ventricles and SAS compartments. This behavior can not be confirmed in clinical studies, as the system is adapted all along life, and we will not be able to see if a compartment is preferred in this case. On the other hand, to see this effect, we should accelerate or slow down heart rate of people during the examination, which is not possible for ethical reasons.

3.2. Pathological case

To confirm that our approach is relevant, we want to verify that if the inputs are given, outputs are close to measurements. In this section, all the parameters are set from MRI acquisition [4]

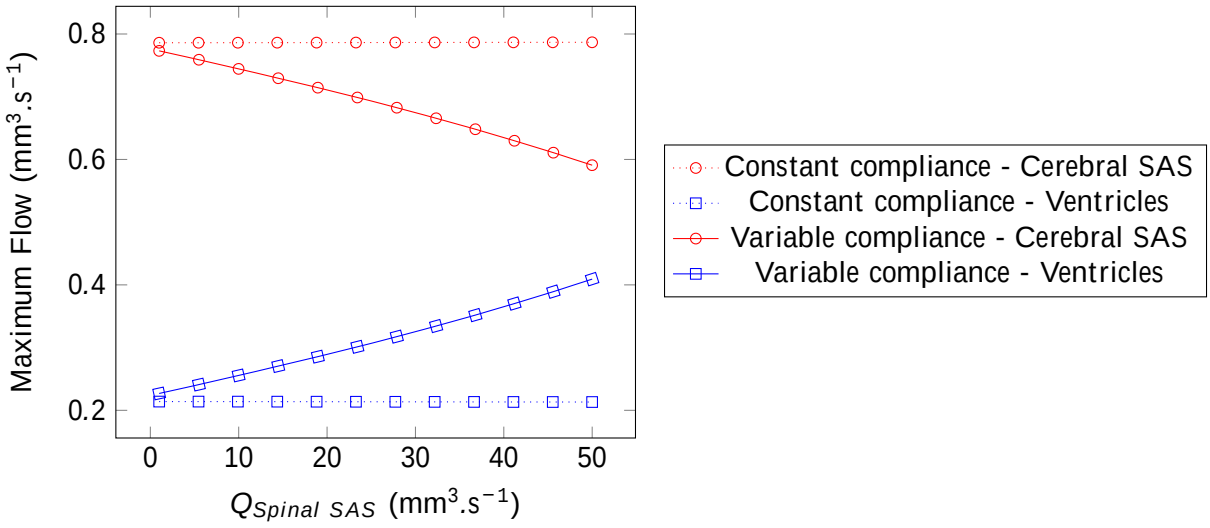

Figure 3.2. $Q_{SAS}^{N,max}$ and $Q_{Vent}^{N,max}$ function of $Q_{SpinalSAS}$.

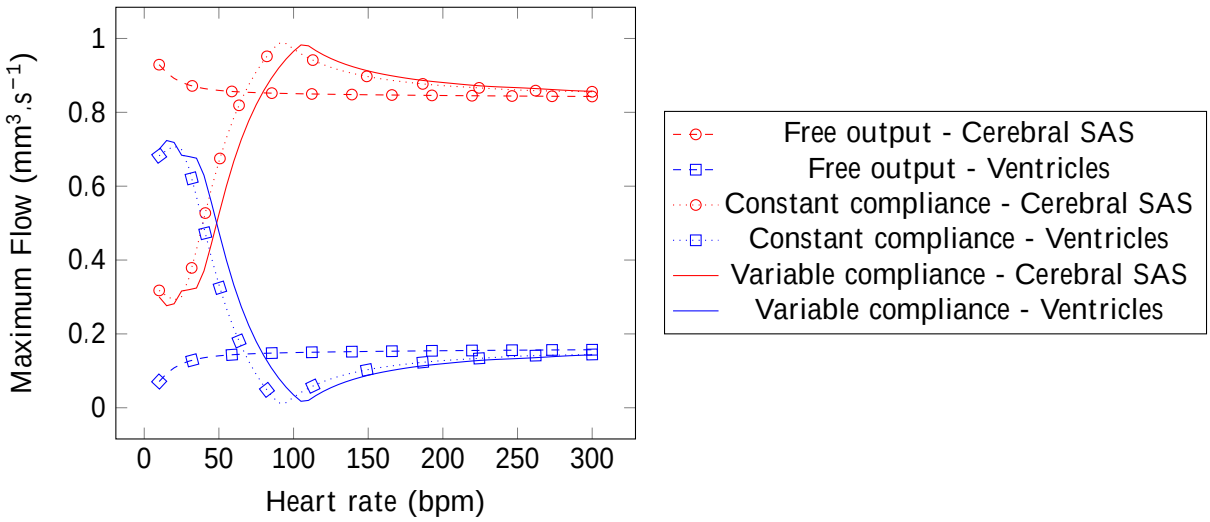

Figure 3.3. $Q_{SAS}^{N,max}$ and $Q_{Vent}^{N,max}$ function of $\omega_{SpinalSAS}$.

and injection test. From morphological MRI, we compute the ratio of volume contained in the cerebral ventricles to the volume contained in the cerebral SAS, and we build the mesh geometry using measurements made with MIPAV software [18], see Fig. 3.4.

The CSF flow curve at the C2–C3 level, see Fig. 3.5(a), imposed at the input and the arterio-venous volume (arterial minus venous volumes), see Fig. 3.5(b), needed in the Windkessel boundary conditions are obtained from PC-MRI.

Remark 3.1. The computed values of the Reynolds number and the Strouhal number are in this case $Re = 7.97$ and $St = 8.29$ in the inlet pipe.

Compliance values are chosen to obtain a global compliance at rest of 1.42 mm^3.Pa^{-1}, which is measured from injection test. This global compliance is divided into $C_{Vent} = {}^1/_4 \times 1.42$ and $C_{Cerebral\ SAS} = {}^3/_4 \times 1.42$ to obtain a representative behavior (in terms of flow) of the cerebrospinal system. The determination of local compliance values from global compliance value is still an open problem. Initial pressure P_0 is taken close to the physiological value of

Figure 3.4. Pathological case. Resulting mesh using real geometry parameters.

(a) CSF ow (b) Arterio-venous volume

Figure 3.5. Pathological case. (a). Measured CSF ow at the C2 C3 level. (b). Calculated arterio-venous volume from PC-MRI.

12 mmHg [8] and the k parameter is de ned as $k = {}^{2:6}\!=_{(C^0_{SAS} + C^0_{V\,ent})}$ to obtain a representative behavior in terms of pressure.

Flow and pressure are shown in Fig. 3.6 (a)-(b). Flow distribution is close to measured ow, as expected, see Fig. 3.7 (a)-(b). Cerebral ventricles ow represents 25% of the spinal SAS ow whereas cerebral SAS ow represents 75%. We can observe the phase shift between maximum ow in the SAS and maximum ow in the ventricles, which is also an expected behavior. Pressure curve is globally similar to the measured intracranial pressure curve, with an heart rate synchronized pulse and a 2.8 mmHg pulse amplitude. However, it does not present peaks and valleys as the one measured, see Fig. 3.7.

3.3. Healthy case

As previously, we want to con rm that outputs are reasonable. But in this section, an injection test can not be done, considering morbidity of a surgical act on healthy people. Consequently, we design the cerebral SAS and cerebral ventricles compliances to obtain a pressure amplitude between 1 mmHg and 3 mmHg, that corresponds to physiological values [21, 1].

Cerebral ventricles compliance is taken equal to $C_{V\,ent} = {}^{1}\!=_{20}$ 4 and the cerebral SAS one to $C_{SAS} = {}^{19}\!=_{20}$ 4 in order to obtain the correct ow distribution. All other parameters are the same as the pathological case.

(a) Flow (b) Pressure

Figure 3.6. Pathological case. (a) Flow. (b) Pressure. All curves are plotted during more than two cardiac cycles.

(a) Flow (b) Pressure

Figure 3.7. Pathological case. (a) Comparison between measured ow and computed ow (b) Comparison between measured pressure and computed pressure.

Remark 3.2. The computed values of the Reynolds number and the Strouhal number are in this case$Re = 23{:}21$ and $St = 4{:}10$ in the inlet pipe.

Flow and pressure are shown in Fig. 3.9 (a)-(b). Flow curve corresponds to physiological behavior, pressure curve has also a physiological amplitude, see Fig. 3.10. Again, phase shift between SAS maximum ow and ventricles maximum ow is observed. But pressure curve does

Figure 3.8. Healthy case. Resulting mesh using real geometry parameters.

(a) Flow (b) Pressure

Figure 3.9. Healthy case. (a) Flow. (b) Pressure. All curves are plotted during more than two cardiac cycles.

not present peaks and valleys as observed in clinical studies for healthy cases, see Fig. 3.11. We can also observe that ow distribution is di erent in the pathological and healthy case: ventricles ow is higher in the pathological case and SAS ow is smoother in the pathological case. The main noticeable di erence between both cases is the value of the global compliance, which is almost four times bigger in the healthy case. It suggests that, for this patient, a loss of compliance of the system is at the origin of the alteration of the CSF dynamics. Moreover, the compliance should be distributed di erently in pathological and healthy case to retrieve the expected ow curve. Ventricles have a proportionally bigger compliance in the pathological case.

Figure 3.10. **Healthy case.** Comparison between measured flow and computed flow.

Figure 3.11. **Healthy case.** Healthy pressure curve form, Cardoso clinical study [7].

Remark 3.3. Differences between pathological and healthy cases are not due to the geometry differences. As the Windkessel models are imposed at the outlets (ventricles and cerebral SAS), geometry has little impact contrarywise to the free output case.

4. Conclusion

A computational model for the cerebrospinal system in a simplified geometry was presented, taking into account the rapid dynamics of the CSF synchronized on the cardiac pulse. The equations solved are the Stokes equations with non-standard boundary conditions, in a bifurcation representative of the different compartments containing the CSF. The non-standard boundary conditions allows to model the confined environment and the arterio-venous volume by using compliances.

The validation of the model is carried out for constant and pulsatile flows. As expected, we have also proved that the rapid dynamics of the CSF can have an impact on the distribution of the fluid in the cerebral ventricles and the SAS. Results of this simplified model with physiological data are in accordance with the physiological behavior of the cerebrospinal system (which is

not the case for a simulation without the Windkessel model). Results equally highlight a large difference of elasticity (and its distribution between compartments) between an healthy and a pathological case, that may be a possible cause of idiopathic hydrocephalus development. This conclusion should be confirmed by some more tests on data available in the BioFlowimage laboratory.

However, the parameters, as the compliance appearing in the lumped model parameters, remain difficult to determine. The compliance values setting need to be improved in order to avoid an injection test, which is an invasive measurement of the ICP. Moreover, the compliance calculated with an injection test is global: it should be divided to obtain cerebral SAS and cerebral ventricles compliance, which is done by tuning the value, in order to obtain a good concordance with the flow curve for the moment. MR elastography could provide an efficient way to better estimate these parameters. Moreover, the numerical pressure curves are not satisfactory, this is clearly a limitation of our approach. In a further study, the numerical model will be improved to remove the compliance estimation problem ([10], [11]).

Acknowledgement

This research was partially funded by the French *Agence Nationale de la Recherche* (Grant Agreement ANR-12-MONU-0010).

References

[1] M.J. Albeck, S.E. Børgesen, F. Gjerris, J.F. Schmidt, and P.S. Sørensen. Intracranial pressure and cerebrospinal fluid outflow conductance in healthy subjects. *J. Neurosurg.*, 74(4):597–600, 1991.

[2] N. Alperin, M. Mazda, T. Lichtor, and S.H. Lee. From cerebrospinal fluid pulsation to noninvasive intracranial compliance and pressure measured by MRI flow studies. *Curr. Med. Imaging Rev.*, 2(1):117–129, 2006.

[3] O. Balédent, C. Gondry-Jouet, M.E. Meyer, G. De Marco, D. Le Gars, M.C. Henry-Feugeas, and I. Idy-Peretti. Relationship between cerebrospinal fluid and blood dynamics in healthy volunteers and patients with communicating hydrocephalus. *Invest. Radiol.*, 39(1):45–55, 2004.

[4] O. Balédent, I. Idy-Peretti, and MC Henry-Feugeas. Cerebrospinal fluid dynamics and relation with blood flow: a magnetic resonance study with semiautomated cerebrospinal fluid segmentation. *Invest. Radiol.*, 36(7):368–377, 2001.

[5] R. Bouzerar, M. Czosnyka, Z. Czosnyka, and O. Balédent. *Physical Phantom of Craniospinal Hydrodynamics*. Springer, 2012.

[6] J. Cahouet and J.-P. Chabard. Some fast 3D finite element solvers for the generalized Stokes problem. *International Journal for Numerical Methods in Fluids*, 8(8):869–895, 1988.

[7] E.R. Cardoso, J.O. Rowan, and S. Galbraith. Analysis of the cerebrospinal fluid pulse wave in intracranial pressure. *J. Neurosurg.*, 59(5):817–821, 1983.

[8] M. Czosnyka and J.D. Pickard. Monitoring and interpretation of intracranial pressure. *J. Neurol. Neurosurg. Psychiatry*, 75(6):813–821, 2004.

[9] J. Fouchet-Incaux, C. Grandmont, and S. Martin. Numerical stability of coupling schemes in the 3D/0D modelling of air flows and blood flows. *HAL-01095960v1*, 2015.

[10] S. Garnotel. *Modélisation numérique de la pression intracrâcranienne via les écoulements du liquide cérébrospinal et du sang mesurés par IRM de flux*. PhD thesis, UPJV, 2016.

[11] S. Garnotel, S. Salmon, and O. Balédent. Numerical cerebrospinal system modeling in fluid- structure interaction. *HAL-01427455*, 2017.

[12] D. Greitz. Radiological assessment of hydrocephalus: New theories and implications for therapy. *Neurosurg. Rev.*, 27(3):145–165, 2004.

[13] F. Hecht. New development in Freefem++. *J. Numer. Math.*, 20(3-4):251–265, 2012.

[14] A.A. Linninger, M. Xenos, D.C. Zhu, M.R. Somayaji, S. Kondapalli, and R.D. Penn. Cerebrospinal fluid flow in the normal and hydrocephalic human brain. *IEEE Trans. Biomed. Eng.*, 54(2):291–302, 2007.

[15] A. Marmarou, M. Bergsneider, N. Relkin, P. Klinge, and P. Black. Development of guidelines for idiopathic normal-pressure hydrocephalus: introduction. *Neurosurgery*, 57(3):S2–1, 2005.

[16] A. Marmarou, K. Shulman, and J. LaMorgese. Compartmental analysis of compliance and outflow resistance of the cerebrospinal fluid system. *J. Neurosurg.*, 43:523–534, 1975.

[17] A. Marmarou, K. Shulman, and R.M. Rosende. A nonlinear analysis of the cerebrospinal fluid system and intracranial pressure dynamics. *J. Neurosurg.*, 48(3):332–344, 1978.

[18] M. McAuliffe. Medical image processing, analysis, and visualization (MIPAV). *National Institutes of Health*, 2009.

[19] G. Pagé, S. Fall, R. Bouzerar, A. Heintz, S. Delepierre, and O. Balédent. In-vitro assessment of high resolution PC-MRI. In *ECR 2015*, 2015.

[20] A. Quarteroni. *Numerical Models for Differential Problems*, volume 2. Springer, 2009.

[21] S. Qvarlander, B. Lundkvist, L.-O D. Koskinen, J. Malm, and A. Eklund. Pulsatility in CSF dynamics: pathophysiology of idiopathic normal pressure hydrocephalus. *J. Neurol. Neurosurg. Psychiatry*, 84(7):735–741, 2013.

[22] J.E. Roberts and J.M. Thomas. Mixed and hybrid methods. *Handb. Numer. Anal.*, 2:523–639, 1991.

[23] K. Sagawa, R.K. Lie, and J. Schaefer. Translation of otto frank's paper "Die Grundform des arteriellen Pulses" Zeitschrift für biologie 37: 483–526 (1899). *J. Mol. Cell. Cardiol*, 22(3):253–254, 1990.

[24] S. El Sankari, C. Gondry-Jouet, A. Fichten, O. Godefroy, J-M. Serot, H. Deramond, M.E. Meyer, O. Balédent, et al. Cerebrospinal fluid and blood flow in mild cognitive impairment and Alzheimer's disease: a differential diagnosis from idiopathic normal pressure hydrocephalus. *Fluids Barriers CNS*, 8(1):12, 2011.

[25] M. Ursino and C.A. Lodi. A simple mathematical model of the interaction between intracranial pressure and cerebral hemodynamics. *J. Appl. Physiol.*, 82(4):1256–1269, 1997.

[26] I.E. Vignon-Clementel, C. A. Figueroa, K. E. Jansen, and C. A. Taylor. Outflow boundary conditions for three-dimensional finite element modeling of blood flow and pressure in arteries. *Computer Methods in Applied Mechanics and Engineering*, 195(29–32):3776 – 3796, 2006.